

ProPINN: Demystifying Propagation Failures in Physics-Informed Neural Networks

Haixu Wu, Yuezhou Ma, Hang Zhou, Huikun Weng, Jianmin Wang, Mingsheng Long[✉]

School of Software, BNRist, Tsinghua University, China

{wuhaixu98}@gmail.com, {mayz20, zhou-h23, wenghk22}@mails.tsinghua.edu.cn

{jimwang, mingsheng}@tsinghua.edu.cn

Abstract

Physics-informed neural networks (PINNs) have earned high expectations in solving partial differential equations (PDEs), but their optimization usually faces thorny challenges due to the unique derivative-dependent loss function. By analyzing the loss distribution, previous research observed the *propagation failure* phenomenon of PINNs, intuitively described as the correct supervision for model outputs cannot “propagate” from initial states or boundaries to the interior domain. Going beyond intuitive understanding, this paper provides a formal and in-depth study of propagation failure and its root cause. Based on a detailed comparison with classical finite element methods, we ascribe the failure to the conventional single-point-processing architecture of PINNs and further prove that propagation failure is essentially caused by the lower *gradient correlation* of PINN models on nearby collocation points. Compared to superficial loss maps, this new perspective provides a more precise quantitative criterion to identify where and why PINN fails. The theoretical finding also inspires us to present a new PINN architecture, named ProPINN, which can effectively unite the gradients of region points for better propagation. ProPINN can reliably resolve PINN failure modes and significantly surpass advanced Transformer-based models with 46% relative promotion.

1 Introduction

Accurately solving physics equations is essential to both scientific and engineering domains [42, 30]. However, it is usually hard to obtain the analytic solution of PDEs. Therefore, classical numerical methods [32, 10] have been widely explored and served as a foundation for modern engineering [1]. Recently, deep models have empowered significant progress in various domains and have also been applied in solving PDEs [37]. As one pioneering progress, physics-informed neural networks (PINNs) are proposed and widely studied [28, 15], which can approximate PDE solutions by formalizing equation constraints, initial and boundary conditions as a loss function and enforcing the outputs and gradients of neural networks to satisfy target PDEs. Taking advantage of the automatic differentiation feature of deep learning frameworks [6, 27], PINN can accurately calculate the derivative without domain discretization, posing a promising direction for solving PDEs.

Although PINNs have attracted great attention, they still face serious challenges in enabling robust training and can fail in some “simple” PDEs, which are called PINN failure modes [22]. Researchers have attempted to tackle the training difficulties with new sampling strategies [45, 9], loss functions [48, 46], optimizers [29], automatic differential methods [31], etc. Especially, Daw et al. [9] noticed a special failure phenomenon during PINN optimization: the interior domain solely optimized by equation constraints will likely converge to a trivial solution. As shown in Figure 1(b), the equation constraint loss of PINN is sufficiently small but the approximated solution is still far from the ground truth. They attributed this to the failure in propagating the supervision of correct solution value from

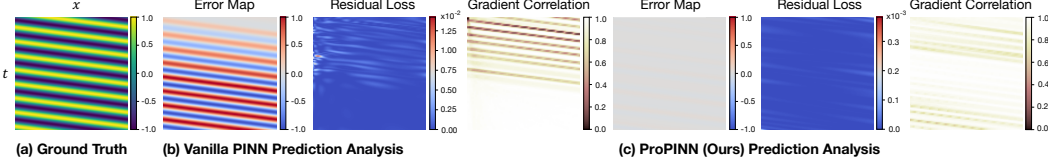


Figure 1: Comparison of PINN and ProPINN on Convection ($\frac{\partial u}{\partial t} + 50 \frac{\partial u}{\partial x} = 0$). In addition to the error map and residual loss, we also plot the gradient correlation of corresponding models between nearby points, which is newly proposed to identify the propagation failure. A low gradient correlation value (the darker color) indicates that the area is hard to propagate. See Appendix A for more results.

initial states or boundaries to interior points, calling it *propagation failure*. Despite this concept seeming intuitive, the formal and rigorous definition of “propagation” processes during the PINN optimization and the root cause of propagation failure are still underexplored.

Some works start from observable loss maps and propose new sampling strategies to accumulate collocation points in areas with high residual losses to break the propagation “barriers” [9, 2]. Although they provide practical remedial measures, these loss-oriented methods may not solve the propagation issue at its root. As illustrated in Figure 1(b), we can find that PINN fails at the beginning according to the actual error map, while the residual loss distribution is too dispersed to identify the beginning failure. To demystify the propagation failure of PINNs, we draw inspiration from traditional numerical methods, which rarely suffer from propagation issues. From the comparison with finite element methods (FEMs) [10], we realize that the primary cause of propagation failure lies in the conventional design principle of PINN model architectures. Unlike FEMs that discretize the input domain as connected meshes, PINNs usually treat the input domain as a set of independently processed collocation points, which makes the optimization of different positions relatively independent, thereby reducing the “interaction” among PINN outputs on nearby positions and resulting in poor propagation.

Based on the above analysis, this paper theoretically proved that the lower *gradient correlation* of PINNs among nearby points is a necessary and sufficient condition for propagation failure. Going beyond the residual loss mainly focused on by previous research [45, 9], gradient correlation provides a foundational understanding of propagation failure, which can serve as a precise criterion to identify propagation issues. For example, in Figure 1(b), the area with the lowest gradient correlation corresponds well to the zone that first appears to have high error. With the idea of enhancing gradient correlation, we present ProPINN as a simple but effective PINN architecture, which can efficiently unite region gradients to boost propagation. ProPINN successfully mitigates the propagation failure and achieves consistent state-of-the-art in various PDEs. Our contributions are summarized as follows:

- Based on a detailed comparison with FEMs, we initially define the *propagation failure* from the model architecture perspective and prove that the root cause of failure is low gradient correlation, which can also serve as a precise criterion to identify PINN failures.
- ProPINN with multi-region mixing mechanism is presented as an efficient architecture, which can tightly unite the optimization of collocation points within a region and theoretically improve the gradient correlation of nearby points for tackling propagation failure in PINNs.
- ProPINN can reliably mitigate PINN failure modes and achieve state-of-the-art with 46% relative gain in typical PDE-solving tasks with favorable efficiency.

2 Preliminaries

A PDE defined in $\Omega \subseteq \mathbb{R}^{d+1}$ with equations \mathcal{F} , initial and boundary conditions \mathcal{I}, \mathcal{B} writes as:

$$\mathcal{F}(u)(\mathbf{x}) = 0, \mathbf{x} \in \Omega; \mathcal{I}(u)(\mathbf{x}) = 0, \mathbf{x} \in \Omega_0; \mathcal{B}(u)(\mathbf{x}) = 0, \mathbf{x} \in \partial\Omega. \quad (1)$$

Here $\mathbf{x} \in \Omega \subseteq \mathbb{R}^{d+1}$ denotes the position information of input points and $u : \mathbb{R}^{d+1} \rightarrow \mathbb{R}^m$ represents the target PDE solution [42, 12]. Usually, $\mathbf{x} = (x_1, \dots, x_d, t)$ contains both spatial and temporal position information and Ω_0 correspond to the $t = 0$ situation. A physics-informed neural network u_θ will approximate the PDE solution u by optimizing the following loss function:

$$\mathcal{L}(u_\theta) = \frac{\lambda_{\text{res}}}{n_{\text{res}}} \sum_{i=1}^{n_{\text{res}}} \|\mathcal{F}(u_\theta)(\mathbf{x}_{\text{res}}^i)\|^2 + \frac{\lambda_{\text{ic}}}{n_{\text{ic}}} \sum_{i=1}^{n_{\text{ic}}} \|\mathcal{I}(u_\theta)(\mathbf{x}_{\text{ic}}^i)\|^2 + \frac{\lambda_{\text{bc}}}{n_{\text{bc}}} \sum_{i=1}^{n_{\text{bc}}} \|\mathcal{B}(u_\theta)(\mathbf{x}_{\text{bc}}^i)\|^2, \quad (2)$$

where λ_* and n_* represent the loss weights and the numbers of collocation points respectively [28].

Propagation failures Unlike the conventional supervised learning that directly constrains the model output, the residual loss (\mathcal{F} item in Eq. (2)) only describes the derivative relation on different positions in Ω (e.g. $\frac{\partial u_\theta}{\partial x_i}$, $\frac{\partial u_\theta}{\partial t}$) and the direct supervision for model outputs $u_\theta(\mathbf{x})$ only exists on initial state Ω_0 or boundaries $\partial\Omega$. For interior points, only constraining model’s gradients without any supervision for the model output may lead to a trivial solution. For example, without considering initial and boundary conditions, the all-zero function $u_\theta = 0$ is also a solution for the convection equation $\frac{\partial u_\theta}{\partial t} + 50\frac{\partial u_\theta}{\partial x} = 0$. Thus, *propagation failure* is proposed by Daw et al. [9]. Their key idea is that to obtain a correct solution in the whole domain, the correct supervision of model outputs must propagate from the initial or boundary points to the interior domain during training. Although Daw et al. [9] provided an intuitive description of why propagation fails in PINN by analyzing the loss distribution, a formal and in-depth understanding of the root cause of propagation failure is still underexplored, which is formally proved in our paper from the model architecture perspective.

Training strategies To tackle optimization challenges of PINNs, training strategies have been widely explored, which can be roughly categorized into the following two branches.

The first branch focuses on sampling strategies to calibrate collocation points at each iteration. These works mainly focus on the areas with high residual loss [22, 36, 45, 2]. Especially, to mitigate the propagation failure described above, R3 [9] is proposed by accumulating sampled collocation points around the high-residual area to break propagation “barriers”. However, all these methods primarily attempt to remedy propagation failure by sampling points, overlooking the inherent deficiency of PINN architecture: independent optimization among points, which is explored in depth by our work.

Besides, PINN loss contained multiple components (Eq. (2)), making loss reweighting essential. Wang et al. [41] proposes to adjust λ_* to balance the convergence rate of different loss components. Considering the temporal causality of PDEs, causal PINN [39] is presented to increase the loss weights of points in the subsequent based on the accumulated residual of previous time steps. Unlike these methods, we focus on the model architecture, which is orthogonal to these loss-oriented works.

Model architectures Vanilla PINN [28] is essentially a multilayer perception (MLP). Afterward, QRes [7] and FLS [44] enhance the model capacity and position embedding respectively. Further, PirateNet [38] leverages residual networks for better scalability. However, all of these methods still process collocation points independently, overlooking spatiotemporal correlations of PDEs. Recently, PINNsFormer [49] first introduced Transformer [35] to PINNs and adopted the attention mechanism to capture temporal correlations among different points. Subsequently, SetPINN [26] extends Transformer to a general spatiotemporal framework. Unlike these models, our proposed ProPINN stems from the in-depth study of propagation failures without relying on the computation-intensive Transformer backbone, achieving better performance and efficiency.

3 Method

As aforementioned, we focus on the *propagation failure* of PINNs, which is one of the foundation problems of PINN optimization. This section will first discuss the propagation properties of PINNs, where we take insights from FEMs to give an intrinsic understanding of why propagation failures exist. Based on theoretical results, we present ProPINN as a simple but effective PINN architecture, which achieves favorable propagation by uniting region gradients. All the proofs are in Appendix C.

3.1 Demystify Propagation Failure

Previous work [9] attributed the propagation failure to “some collocation points start converging to trivial solutions before the correct solution from initial/boundary points is able to reach them.” However, we find that, in FEMs, the iteration will start from a trivial estimation and the interior areas also hold incorrect output supervision in the beginning iterations, while they present quite robust performance and do not affect by propagation issues. Thus, beyond direct and intuitive understandings, we believe there exists an unexplored root cause for propagation failures.

To demystify propagation failures of PINNs, we make a detailed comparison between FEMs and PINNs on their parameter updating processes. As presented in Figure 2, the parameters of FEMs

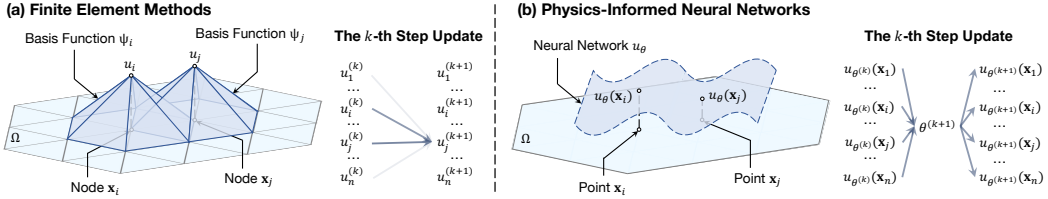


Figure 2: Comparison between (a) FEMs and (b) PINNs. Blue arrows highlight quantities with direct interactions during training. Compared to FEMs, solution values of PINNs among different positions are under an implicit correlation by updating model parameter θ during training.

are defined on discretized mesh points and nearby points will directly affect each other during optimization, which can be formally stated as follows.

Theorem 3.1 (Propagation in FEMs). [10] Suppose that FEMs discretize Ω into computation meshes with n nodes $\{\mathbf{x}_i\}_{i=1}^n$ and approximate the PDE solution by optimizing coefficients of basis functions $\{\Psi_i\}_{i=1}^n$, which are defined as region linear interpolation. Denote the coefficient of basis function Ψ_i as u_i , which is also the solution value of the i -th node. With the Jacobi iterative method for solution value update, the interaction among solution values $\{u_i\}_{i=1}^n$ at the k -th step is:

$$u_j^{(k+1)} = \frac{1}{D(\Psi_j, \Psi_j)} \left(b_j - \sum_{i \neq j} D(\Psi_i, \Psi_j) u_i^{(k)} \right), \quad (3)$$

where $\{b_j\}_{j=1}^n$ are constants related to external force. $D(\cdot, \cdot)$ is a variational version of PDE equation $\mathcal{F}(\cdot)$, which presents non-zero values only for overlapped basis functions.

Remark 3.2 (FEMs are under active propagation). Theorem 3.1 demonstrates that coefficients of basis functions with overlap area are explicitly correlated. Thus, the change of $u_i^{(k)}$ will directly affect the value of its adjacent nodes, ensuring an active propagation among the whole domain.

Remark 3.3 (Physical meanings of Eq. (3)). The parameter update in FEMs relies on $D(\cdot, \cdot)$, which is also named as stiffness matrix in solid mechanics [47]. $D(\Psi_i, \Psi_j)$ describes the force on the j -th node to make region balance when the i -th node has a unit displacement.

Inspired by analyses of FEMs, we define the propagation in PINNs in terms of the influence of each point's value change on other points, yielding the first formal measurement of the propagation failure. Since in PINNs, the model output is determined by model parameter θ , we propose to represent “value change” from the gradient perspective, namely $\left. \frac{\partial u_\theta}{\partial \theta} \right|_{\mathbf{x}}$. This perspective help us redefines the stiffness matrix from FEMs [47] in the context of PINN models, bridging the computation gap between PINNs and FEMs. Specifically, the propagation failure of PINNs can be defined as follows.

Definition 3.4 (Propagation failure in PINN). In spirit of the physics meaning of Eq. (3), we define the “stiffness” coefficient between \mathbf{x} and \mathbf{x}' for PINN u_θ as the “slope” w.r.t. the parameter change:

$$D_{\text{PINN}}(\mathbf{x}, \mathbf{x}') = \lim_{\lambda \rightarrow 0} \frac{\left\| u_\theta(\mathbf{x}') - u_{\theta - \lambda \left. \frac{\partial u_\theta}{\partial \theta} \right|_{\mathbf{x}}}(\mathbf{x}') \right\|}{\lambda}, \quad (4)$$

which measures the impact on model output at \mathbf{x}' after updating PINN with a unit step at \mathbf{x} . This formula is analogous to applying a unit force at \mathbf{x} and observing a displacement at \mathbf{x}' . If \mathbf{x} and \mathbf{x}' are adjacent and $D_{\text{PINN}}(\mathbf{x}, \mathbf{x}')$ is less than an empirically defined threshold ϵ , we consider that propagation failure has occurred between \mathbf{x} and \mathbf{x}' .

Remark 3.5 (Region propagation). In FEMs (shown in Figure 2(a)), only overlapped basis functions (corresponding to adjacent discretization points) could have a non-zero stiffness coefficient. Thus, we only discuss propagation among nearby points in the definition of Eq. (4).

Based on the above formal definition, we can further derive the root cause for propagation failures of PINNs, which transforms the physical-meaning-based definition into a deep model property.

Theorem 3.6 (Gradient correlation). Given a PINN u_θ and adjacent points $\mathbf{x}, \mathbf{x}' \in \Omega$, the necessary and sufficient condition of propagation failure between \mathbf{x} and \mathbf{x}' is a small gradient correlation, which is formally defined as follows

$$G_{u_\theta}(\mathbf{x}, \mathbf{x}') = \left\| \left\langle \left. \frac{\partial u_\theta}{\partial \theta} \right|_{\mathbf{x}}, \left. \frac{\partial u_\theta}{\partial \theta} \right|_{\mathbf{x}'} \right\rangle \right\|. \quad (5)$$

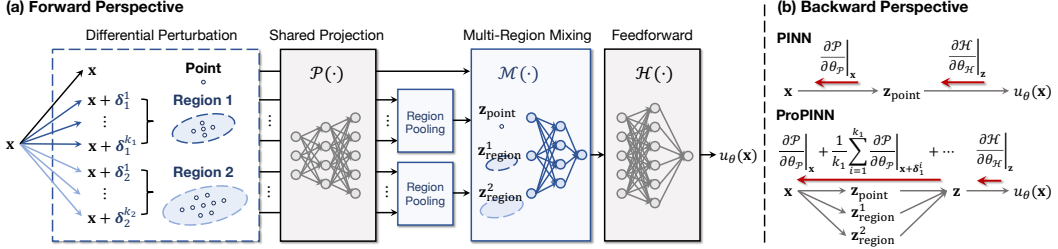


Figure 3: Overall architecture of ProPINN from both (a) forward and (b) backward perspectives, where the single input point is augmented to point sets in multiscale regions, which can efficiently unite model parameter gradients on different positions within multiple regions.

Why propagation failures exist in PINNs According to the definition of Eq. (5), the gradient correlation is an inner product of high-dimensional tensors, where $\frac{\partial u_\theta}{\partial \theta}|_* \in \mathbb{R}^{m \times |\theta|}$, $|\theta|$ denotes the parameter size (usually $> 10^3$) and m is the output dimension. Thus, these gradient tensors are easy to be orthogonal in the high-dimensional space [3], especially when different positions are independently optimized. For example, position \mathbf{x} and position \mathbf{x}' could correspond to different parts of model parameters. Further, this analysis also provides insights for “why PINNs cannot benefit from large models” [38], since a larger parameter size $|\theta|$ is more likely to cause orthogonal gradients.

3.2 Propagation Physics-Informed Neural Networks

Theorem 3.6 highlights that the gradient correlation is the foundation item that affects the propagation of PINNs. Note that the gradient correlation is essentially determined by the model architecture. Thus, we present ProPINN as a new PINN architecture to enhance the gradient correlation by introducing unified region gradient to each collocation point, which can effectively boost the propagation.

As shown in Figure 3, the key component of ProPINN is a multi-region mixing mechanism, which is a well-thought-out design considering both efficiency and performance. Here are the details.

Differential perturbation Given a single collocation point $\mathbf{x} \in \Omega \subseteq \mathbb{R}^{(d+1)}$, we first augment it by perturbing its position within multiscale regions. Note that different from PINNsFormer [49] and SetPINN [26] that only utilize augmented representations of multiple points but detach the gradient backpropagation, ProPINN leverages the perturbation as a differential layer and projects all the augmented points into deep representations with a shared projector $\mathcal{P}(\cdot)$, which is:

$$\text{Diff-Aug}(\mathbf{x}) = \left\{ \mathbf{x}, \left\{ \{\mathbf{x} + \delta_r^i\}_{i=1}^{k_r} \right\}_{r=1}^{\#\text{scale}} \right\},$$

$$\mathbf{z}_{\text{point}} = \mathcal{P}(\mathbf{x}), \left\{ \mathbf{z}_{\text{region}}^{i,r} \right\}_{i=1}^{k_r} = \left\{ \mathcal{P}(\mathbf{x} + \delta_r^i) \right\}_{i=1}^{k_r} \quad (6)$$

where $\{\delta_r^i\}_{i=1}^{k_r}$ are random perturbations for \mathbf{x} within the r -th region whose size is $[-R_r, R_r]^{d+1}$, and k_r is the corresponding number of perturbations. We denote the number of scales, i.e., the number of multiscale regions, as $\#\text{scale}$. $\mathbf{z}_{\text{point}}, \mathbf{z}_{\text{region}}^{i,r} \in \mathbb{R}^{d_{\text{model}}}$ are representations of the original point \mathbf{x} and its multi-region augmentation $(\mathbf{x} + \delta_r^i)$ respectively. $\mathcal{P} : \mathbb{R}^{d+1} \rightarrow \mathbb{R}^{d_{\text{model}}}$ is a lightweight MLP to encode the coordinates of collocation and augmented points. Notably, the design in considering different-scale regions not only covers multiscale properties of PDEs but also simulates non-uniform meshes in FEMs, where each point can selectively aggregate information from multiple regions.

From the model forward perspective, the above design can naturally augment the receptive field. Moreover, from the backward perspective shown in Figure 3(b), the differential perturbation design can also aggregate gradients of collocation points within multiscale regions, thereby enhancing the gradient correlation on projection parameter $\theta_{\mathcal{P}}$ among adjacent points.

Multi-region mixing After shared projection, we can obtain $(1 + \sum_{r=1}^{\#\text{scale}} k_r)$ representations from multi-region augmented positions. Previous Transformer-based studies, such as PINNsFormer [26] and SetPINN [26], apply the attention mechanism [35] among collocation points to capture complex spatiotemporal dependencies. However, since attention involves inner products among

representations, it will also bring huge computation costs in both forward and backpropagation processes, especially for PINNs that usually need to calculate high-order gradients.

Instead of directly modeling dependencies among collocation points, we propose an efficient multi-region mixing mechanism. It first averages the representations in various regions to generate multiple region representations. Owing to the special property of PDEs, the pooled multiscale representations are still under the same PDE but with different coefficients [14]. Thus, compared to complex dependencies among different positions, the relation among different coefficient PDEs is much more steady, allowing us to adopt a simple linear mixing layer rather than the attention mechanism:

$$\begin{aligned} \mathbf{z}_{\text{region}}^r &= \text{Pooling} \left(\left\{ \mathbf{z}_{\text{region}}^{i,r} \right\}_{i=1}^{k_r} \right), r = 1, \dots, \#\text{scale} \\ \mathbf{z} &= \mathcal{M} (\mathbf{z}_{\text{point}}, \mathbf{z}_{\text{region}}^1, \dots, \mathbf{z}_{\text{region}}^{\#\text{scale}}), \end{aligned} \quad (7)$$

where $\mathcal{M} : \mathbb{R}^{(1+\#\text{scale}) \times d_{\text{model}}} \rightarrow \mathbb{R}^{d_{\text{model}}}$ is an MLP layer for mixing multi-region representations. Afterward, the mixed representation \mathbf{z} is projected to the target dimension by another MLP layer $\mathcal{H} : \mathbb{R}^{d_{\text{model}}} \rightarrow \mathbb{R}^m$ which eventually generates the PDE solution, namely $u_{\theta}(\mathbf{x}) = \mathcal{H}(\mathbf{z}) \in \mathbb{R}^m$.

Gradient analysis As presented in the visualization of Figure 1 (c), by uniting region gradients, ProPINN can successfully boost the gradient correlation for better propagation, which can also be theoretically understood through the following theorem.

Assumption 3.7 (Correlation among region gradients). *Given PINN u_{θ} , we assume that there exists a region size $R > 0$, s.t. $\forall \mathbf{x}, \mathbf{x}' \in \Omega$ with $\|\mathbf{x} - \mathbf{x}'\| \leq R$, $\left\langle \frac{\partial u_{\theta}}{\partial \theta} \Big|_{\mathbf{x}}, \frac{\partial u_{\theta}}{\partial \theta} \Big|_{\mathbf{x}'} \right\rangle \geq 0$.*

Theorem 3.8 (Gradient correlation improvement). *Under Assumption 3.7 with region size R , given k perturbations $\{\delta_i\}_{i=1}^k$ with $\|\delta_i\| \leq \frac{R}{3}$ and defining $u_{\theta}^{\text{region}}(\mathbf{x}) = u_{\theta}(\mathbf{x}) + \frac{\sum_{i=1}^k u_{\theta}(\mathbf{x} + \delta_i)}{k}$, then $\forall \mathbf{x}, \mathbf{x}' \in \Omega$, if $\|\mathbf{x} - \mathbf{x}'\| \leq \frac{R}{3}$, we have $G_{u_{\theta}}(\mathbf{x}, \mathbf{x}') \leq G_{u_{\theta}^{\text{region}}}(\mathbf{x}, \mathbf{x}')$.*

Remark 3.9 (Efficient design in ProPINN). *Theorem 3.8 demonstrates that aggregating region points by differential perturbation (Eq. (6)) can enhance the gradient correlation of nearby points. Considering the efficiency, ProPINN limits the region aggregation only within the lightweight projection layer \mathcal{P} instead of the whole model, which can already effectively avoid propagation failure.*

Efficiency analysis Compared to single-point-processing architectures, the extra computation of ProPINN comes from augmentation in Eq. (6). Supposed that flops of $\mathcal{P}(\cdot)$ is $\text{ops}(\mathcal{P})$, the extra cost of ProPINN is $\sum_{r=1}^{\#\text{scale}} k_r \text{ops}(\mathcal{P})$. Although this seems like a large overload, it will not affect the efficiency of ProPINN significantly in practice. This efficiency benefits from the parallel computation in both forward and backward computation graphs [27], as well as the lightweight design of the projection layer (\mathcal{P}). In our experiments, ProPINN is 2-3× faster than other explicit dependency modeling methods (e.g. PINNsFormer [49] and SetPINN [26]) and comparable with other single-point-processing PINNs (e.g. QRes [7] and FLS [44]) but with 60%+ relative error reduction.

4 Experiments

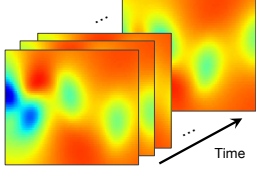
We widely test ProPINN in extensive PDE-solving tasks and provide detailed comparisons with advanced PINN architectures in performance, efficiency and scalability. More visualization analyses and all the implementation details can be found in Appendix A-D.

Benchmarks As listed in Table 1, we experiment with six PDE-solving tasks, covering diverse 1D and 2D time-dependent PDEs. Specifically, solutions of Convection, 1D-Reaction and Allen-Cahn contain some steep areas, which are challenging to approximate and have been used to demonstrate PINN failure modes [22] and propagation failures [9]. Besides, 1D-Wave involves second-order derivatives, making it hard to optimize. In addition to the above standard benchmarks, we also test ProPINN with extremely challenging fluid dynamics, which are governed by intricate Navier-Stokes equations [8]. *Karman Vortex* is from [28], which describes the fluid dynamics around a cylinder, exhibiting the famous Karman vortex street [43]. *Fluid Dynamics* is from [40] and involves fast dynamics of fluid on a torus. More benchmark details can be found in Appendix D.1.

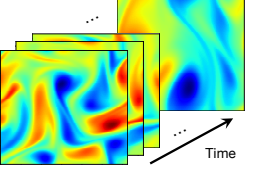
Baselines In addition to vanilla PINN [28], we also compare ProPINN with other six PINN architectures. QRes [7], FLS [44], KAN [24] and PirateNet [38] are under the conventional PINN

Table 1: Summary of benchmarks, covering both standard PDE-solving tasks and complex fluid dynamics. #Dim denotes the dimension of input domain, “+T” refers to “time-dependent”. We also visualize target solutions in (a) Karman Vortex and (b) Fluid Dynamics tasks, which involve complex spatiotemporal dynamics and multi-physics (velocity and pressure) interactions in the 2D+T space.

Type	#Dim	Benchmarks		Property
Standard Tasks	1D+T	Convection		
		1D-Reaction		
		Allen-Cahn	[22]	
Complex Fluid	2D+T	1D-Wave	High-order	
		Karman Vortex		
		Fluid Dynamics	Navier-Stokes	



(a) Karman Vortex



(b) Fluid Dynamics

Table 2: Performance comparison of different PINN architectures on standard PDE-solving tasks, which usually appear failure modes [22]. Both rMAE and rRMSE are recorded. Smaller values indicate better performance. For clarity, the best result is in bold and the second best is underlined. Promotion refers to the relative error reduction w.r.t. the second best model ($1 - \frac{\text{Our error}}{\text{The second best error}}$).

Model	Convection		1D-Reaction		Allen-Cahn		1D-Wave	
	rMAE	rRMSE	rMAE	rRMSE	rMAE	rRMSE	rMAE	rRMSE
Vanilla PINN [28]	0.778	0.840	0.982	0.981	0.350	0.562	0.326	0.335
QRes [7]	0.746	0.816	0.979	0.977	0.942	0.946	0.523	0.515
FLS [44]	0.674	0.771	0.984	0.985	0.357	0.574	0.102	0.119
KAN [24]	0.922	0.954	0.031	0.061	0.352	0.563	0.499	0.489
PirateNet [38]	1.169	1.287	0.017	0.044	0.098	0.179	0.051	0.055
PINNsFormer [49]	<u>0.023</u>	<u>0.027</u>	<u>0.015</u>	<u>0.030</u>	0.331	0.529	0.270	0.283
SetPINN [26]	0.028	0.033	0.018	0.034	0.381	0.601	0.347	0.353
ProPINN (Ours)	0.018	0.020	0.010	0.020	0.036	0.087	0.016	0.016
Promotion	22%	26%	33%	33%	63%	51%	69%	71%

architecture, where different collocation points are independently optimized. PINNsFormer [49] and SetPINN [26] are based on the Transformer backbone to capture spatiotemporal correlations among PDEs. PirateNet and PINNsFormer are previous state-of-the-art models. In addition, we also integrate ProPINN with sampling strategy R3 [9], loss reweighting method [41] and the latest optimization algorithm RoPINN [46] to verify that these methods contribute orthogonally to us.

Implementations For all benchmarks, we set the number of regions $\#scale = 3$ with region size $\{R_1, R_2, R_3\} = \{10^{-2}, 5 \times 10^{-2}, 9 \times 10^{-2}\}$, number of perturbations $\{k_1, k_2, k_3\} = \{3^{(d+1)}, 5^{(d+1)}, 7^{(d+1)}\}$ and representation dimension $d_{\text{model}} = 32$. For Convection, 1D-Reaction, Allen-Cahn, 1D-Wave and Karman Vortex, we follow [49] and train the model with L-BFGS optimizer [23] for 1,000 iterations in PyTorch [27]. As for Fluid Dynamics, we follow [40] and experiment with JAX [6]. Relative L1 Error (rMAE) and relative Root Mean Square Error (rRMSE) are recorded.

4.1 Standard Benchmarks

Main results From results presented in Table 2, we can obtain the following key observations.

ProPINN successfully mitigates PINN failure modes in Convection, 1D-Reaction and Allen-Cahn. Its outstanding performance in 1D-Wave also verifies its capability in handling high-order PDEs. Notably, ProPINN also beats the latest Transformer-based models PINNsFormer [49] and SetPINN [26] with 46% rMAE reduction averaged from four PDEs, highlighting the advantage of our method.

It is also observed that only architectures that consider interactions among multiple points (PINNsFormer, SetPINN and ProPINN) consistently work for all four tasks. All the models under the single-point-processing paradigm fail in Convection. This justifies our discussion about the deficiency of single-point architectures, where independent optimization can easily cause propagation failure.

Visualization To clearly compare model capacity in solving PDEs, we also visualize approximated solutions in Figure 4. We can find that PirateNet, under the single-point-processing paradigm, fails in handling the steep variations in Convection. As for the 1D-Wave with high-order derivatives, we

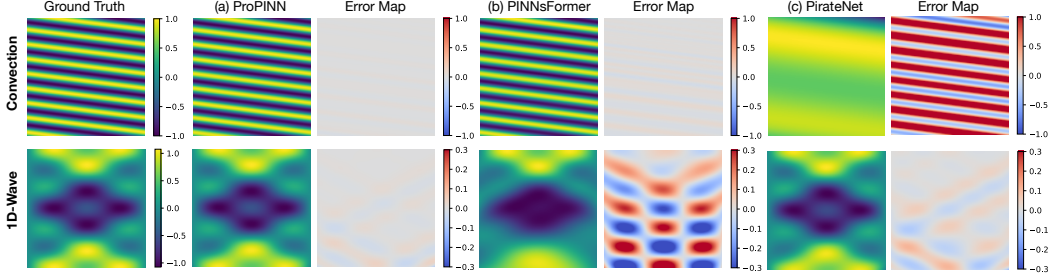


Figure 4: Visualization of model approximated solutions. Error map ($u_\theta - u$) is also plotted.

find that PINNsFormer yields an insufficient performance, which may be because of the optimization difficulty of the attention mechanism under high-order loss. In contrast, ProPINN achieves consistent performance in tackling the above-mentioned challenges, highlighting its effectiveness.

Efficiency comparison To verify the practicability of our method, we also provide the efficiency comparison in Figure 5. It is observed that ProPINN is about 2-3 \times faster than recent Transformer-based models: PINNsFormer [49] and SetPINN [26]. Also, benefiting from our lightweight design for the projection layer and parallel computing, ProPINN is comparable to single-point-processing PINNs in efficiency but brings more than 60%+ error reduction, achieving a favorable performance-efficiency trade-off.

4.2 Complex Physics

As a long-standing mathematical problem, Navier-Stokes equations [34] for fluid dynamics have shown significant challenges and profound importance in real-world applications [11]. Thus, in addition to standard benchmarks, we also experiment with Karman Vortex and Fluid Dynamics, which involve extremely intricate PDEs and spatiotemporal dynamics as shown in Table 1.

Main results Compared to PDEs listed in Table 2, fluid simulation tasks in this section are much more complex. As shown in Table 3, ProPINN still achieves the best performance with over 30% relative promotion on average than the previous best model. Notably, ProPINN performs fairly well in the Fluid Dynamics task, which requires the model to accurately calculate velocity and pressure solutions for the whole spatiotemporal sequence purely based on equation supervision. This task is under rapid and ever-changing dynamics and the last frame is far from its initial state (Table 1 (b)), making it extremely challenging. Besides, we also observe that PINNsFormer and SetPINN suffer from the training instability problem, which confirms our previous discussion on the training difficulties of the attention mechanism, further demonstrating the effectiveness of our MLP-based design in multi-region mixing.

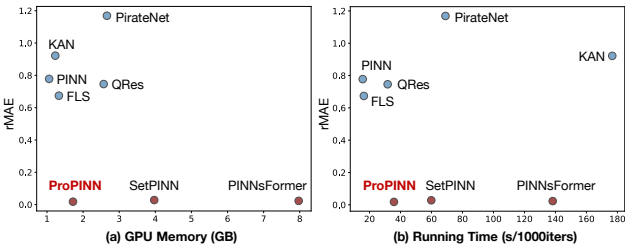


Figure 5: Efficiency comparisons on Convection. Models under the single-point-processing paradigm are colored in blue, while models that consider point correlations are in red. ProPINN achieves the best performance with the lowest error and the lowest running time.

Table 3: Comparison of different PINN architectures in solving 2D time-dependent Navier-Stokes equations. “Nan” indicates that this model encounters the training instability problem. Since Fluid Dynamics is based on JAX [6] and it is hard to transfer the PyTorch implementation of KAN to JAX, we did not test it in this task, labeled in “/”.

Model	Karman Vortex		Fluid Dynamics	
	rMAE	rRMSE	rMAE	rRMSE
Vanilla PINN [28]	13.08	9.08	0.3659	0.4082
QRes [7]	6.41	4.45	0.2668	0.3144
FLS [44]	3.98	2.77	0.2362	0.2765
KAN [24]	1.43	1.25	/	/
PirateNet [38]	1.24	1.16	0.4550	0.5232
PINNsformer [49]	0.384	0.280	Nan	Nan
SetPINN [26]	0.287	0.209	Nan	Nan
ProPINN (Ours)	0.161	0.124	0.1834	0.2172
Promotion	44%	41%	22%	21%

Visualization As presented in Figure 6, ProPINN can accurately simulate the future variations of fluid, including the inner complex vortexes and distortions, even if the future frames are significantly

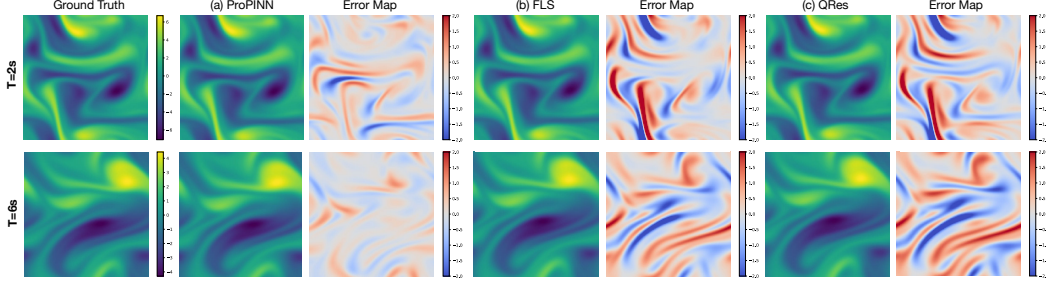


Figure 6: Visualization of the Fluid Dynamics task. Error map ($u_\theta - u$) is also plotted.

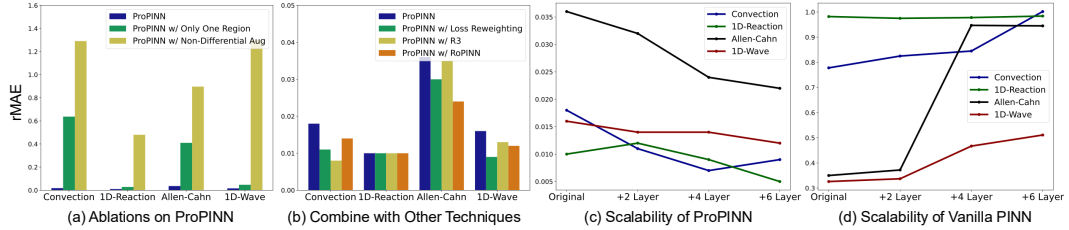


Figure 7: (a) Ablations on multi-region mixing in Eq. (7) and differential perturbation in Eq. (6). (b) Integration with other techniques. (c-d) rMAE changes of ProPINN and PINN when adding layers.

changed. This indicates that ProPINN can give a precise solution for the Navier-Stokes equations, especially in processing the convection term, which is nonlinear and extremely complex.

4.3 Model Analysis

Ablations We provide a detailed ablation in Figure 7(a), including experiments with only one region in Eq. (7), i.e. $\#scale = 1$ and detaching gradients of augmented points in Eq. (6). Results demonstrate that both multi-region mixing and differential perturbation are essential for the final performance. Especially, the non-differential perturbation will seriously damage the model’s performance, even though it utilizes more collocation points to augment the receptive field. This finding further confirms that, compared with augmenting representation, uniting gradients of region points is more important for PINN optimization, verifying that region gradient correlations are the key factor.

Integrating with other strategies As we discussed in related work, ProPINN mainly focuses on architecture design, which is orthogonal to previous research on training strategies. To verify their orthogonal contributions, we integrate ProPINN with the loss reweighting method [41] and sampling strategy R3 [9] and optimization algorithm RoPINN [46]. As illustrated in Figure 7(b), these methods can further boost the performance of ProPINN. As for 1D-Reaction, which is relatively simple, ProPINN’s performance is nearly optimal, thus, the integration does not bring further promotion.

Model scalability Theorem 3.6 attributes the propagation failure to lower region gradient correlations. As we discussed in Remark, since gradient correlation is defined as the inner product of high-dimensional gradient tensors in size $m \times |\theta|$, the correlation is easier to be orthogonal when adding model parameters. Thus, vanilla PINN presents the performance drop in larger models (Figure 7(d)). In contrast, ProPINN successfully mitigates propagation issues by introducing region gradients, which not only tackle PINN failure modes but also empower the model with favorable scalability.

5 Conclusion

This paper focuses on the propagation failures of PINNs and provides a formal and in-depth study of this crucial phenomenon. Going beyond the intuitive understanding, we theoretically proved that the root cause of propagation failures is the lower gradient correlation among nearby points, which can serve as a precise criterion for PINN failures. Inspired by the above theoretical analyses, ProPINN is presented as a new PINN architecture, which can effectively unite the gradients of region points for better propagation. Experimentally, ProPINN can naturally enhance region gradient correlation and achieve remarkable promotion on standard benchmarks and challenging PDE-solving tasks with a favorable trade-off between performance and efficiency, also presenting better scalability.

References

- [1] William F Ames. *Numerical methods for partial differential equations*. Academic press, 2014.
- [2] Anonymous. L-pinn: A langevin dynamics approach with balanced sampling to improve learning stability in physics-informed neural networks. In *Submitted to the 13th ICLR*, 2024. under review.
- [3] Keith Ball. An elementary introduction to modern convex geometry. 1997.
- [4] Martino Bardi, Italo Capuzzo Dolcetta, et al. *Optimal control and viscosity solutions of Hamilton-Jacobi-Bellman equations*. Springer, 1997.
- [5] Feliks Aleksandrovich Berezin and Mikhail Shubin. *The Schrödinger Equation*. Springer Science & Business Media, 2012.
- [6] James Bradbury, Roy Frostig, Peter Hawkins, Matthew James Johnson, Chris Leary, Dougal Maclaurin, George Necula, Adam Paszke, Jake VanderPlas, Skye Wanderman-Milne, and Qiao Zhang. JAX: composable transformations of Python+NumPy programs, 2018.
- [7] Jie Bu and Anuj Karpatne. Quadratic residual networks: A new class of neural networks for solving forward and inverse problems in physics involving pdes. In *SIAM*, 2021.
- [8] Peter Constantin and Ciprian Foiaş. *Navier-stokes equations*. University of Chicago press, 1988.
- [9] Arka Daw, Jie Bu, Sifan Wang, Paris Perdikaris, and Anuj Karpatne. Mitigating propagation failures in physics-informed neural networks using retain-resample-release (R3) sampling. In *ICML*, 2023.
- [10] Gouri Dhatt, Emmanuel Lefrançois, and Gilbert Touzot. *Finite element method*. John Wiley & Sons, 2012.
- [11] Charles R Doering and John D Gibbon. *Applied analysis of the Navier-Stokes equations*. Cambridge university press, 1995.
- [12] Lawrence C Evans. *Partial differential equations*. American Mathematical Soc., 2010.
- [13] Herman H Goldstine, Francis J Murray, and John Von Neumann. The jacobi method for real symmetric matrices. *Journal of the ACM (JACM)*, 1959.
- [14] Ivan G Graham, Patrick O Lechner, and Robert Scheichl. Domain decomposition for multiscale pdes. *Numerische Mathematik*, 2007.
- [15] Zhongkai Hao, Songming Liu, Yichi Zhang, Chengyang Ying, Yao Feng, Hang Su, and Jun Zhu. Physics-informed machine learning: A survey on problems, methods and applications. *arXiv preprint arXiv:2211.08064*, 2022.
- [16] Zheyuan Hu, Khemraj Shukla, George Em Karniadakis, and Kenji Kawaguchi. Tackling the curse of dimensionality with physics-informed neural networks. *Neural Networks*, 2024.
- [17] Zheyuan Hu, Zhouhao Yang, Yezhen Wang, George Em Karniadakis, and Kenji Kawaguchi. Bias-variance trade-off in physics-informed neural networks with randomized smoothing for high-dimensional pdes. *arXiv preprint arXiv:2311.15283*, 2023.
- [18] Arthur Jacot, Franck Gabriel, and Clément Hongler. Neural tangent kernel: Convergence and generalization in neural networks. *NeurIPS*, 2018.
- [19] George Karniadakis and Spencer J Sherwin. *Spectral/hp element methods for computational fluid dynamics*. Oxford University Press, USA, 2005.
- [20] Diederik P. Kingma and Jimmy Ba. Adam: A method for stochastic optimization. In *ICLR*, 2015.
- [21] David A Kopriva. *Implementing spectral methods for partial differential equations: Algorithms for scientists and engineers*. Springer Science & Business Media, 2009.
- [22] Aditi Krishnapriyan, Amir Gholami, Shandian Zhe, Robert Kirby, and Michael W Mahoney. Characterizing possible failure modes in physics-informed neural networks. *NeurIPS*, 2021.
- [23] Dong C Liu and Jorge Nocedal. On the limited memory bfgs method for large scale optimization. *Mathematical programming*, 1989.
- [24] Ziming Liu, Yixuan Wang, Sachin Vaidya, Fabian Ruehle, James Halverson, Marin Soljačić, Thomas Y Hou, and Max Tegmark. Kan: Kolmogorov-arnold networks. *arXiv preprint arXiv:2404.19756*, 2024.

[25] Barnes W McCormick. *Aerodynamics, aeronautics, and flight mechanics*. John Wiley & Sons, 1994.

[26] Mayank Nagda, Phil Ostheimer, Thomas Specht, Frank Rhein, Fabian Jirasek, Marius Kloft, and Sophie Fellenz. Setpinns: Set-based physics-informed neural networks. *arXiv preprint arXiv:2409.20206*, 2024.

[27] Adam Paszke, S. Gross, Francisco Massa, A. Lerer, James Bradbury, Gregory Chanan, Trevor Killeen, Z. Lin, N. Gimelshein, L. Antiga, Alban Desmaison, Andreas Köpf, Edward Yang, Zach DeVito, Martin Raison, Alykhan Tejani, Sasank Chilamkurthy, Benoit Steiner, Lu Fang, Junjie Bai, and Soumith Chintala. Pytorch: An imperative style, high-performance deep learning library. In *NeurIPS*, 2019.

[28] Maziar Raissi, Paris Perdikaris, and George E Karniadakis. Physics-informed neural networks: A deep learning framework for solving forward and inverse problems involving nonlinear partial differential equations. *Journal of Computational physics*, 2019.

[29] Pratik Rathore, Weimu Lei, Zachary Frangella, Lu Lu, and Madeleine Udell. Challenges in training pinns: A loss landscape perspective. *arXiv preprint arXiv:2402.01868*, 2024.

[30] Tomáš Roubíček. *Nonlinear partial differential equations with applications*. Springer Science & Business Media, 2013.

[31] Zekun Shi, Zheyuan Hu, Min Lin, and Kenji Kawaguchi. Stochastic taylor derivative estimator: Efficient amortization for arbitrary differential operators. In *NeurIPS*, 2024.

[32] Pavel Šolín. *Partial differential equations and the finite element method*. John Wiley & Sons, 2005.

[33] Matthew Tancik, Pratul Srinivasan, Ben Mildenhall, Sara Fridovich-Keil, Nithin Raghavan, Utkarsh Singhal, Ravi Ramamoorthi, Jonathan Barron, and Ren Ng. Fourier features let networks learn high frequency functions in low dimensional domains. *NeurIPS*, 2020.

[34] Roger Temam. *Navier-Stokes equations: theory and numerical analysis*. American Mathematical Soc., 2001.

[35] Ashish Vaswani, Noam Shazeer, Niki Parmar, Jakob Uszkoreit, Llion Jones, Aidan N Gomez, Łukasz Kaiser, and Illia Polosukhin. Attention is all you need. In *NeurIPS*, 2017.

[36] Chuwei Wang, Shanda Li, Di He, and Liwei Wang. Is l^2 physics informed loss always suitable for training physics informed neural network? *NeurIPS*, 2022.

[37] Hanchen Wang, Tianfan Fu, Yuanqi Du, Wenhao Gao, Kexin Huang, Ziming Liu, Payal Chandak, Shengchao Liu, Peter Van Katwyk, Andreea Deac, et al. Scientific discovery in the age of artificial intelligence. *Nature*, 2023.

[38] Sifan Wang, Bowen Li, Yuhang Chen, and Paris Perdikaris. Piratenets: Physics-informed deep learning with residual adaptive networks. *arXiv preprint arXiv:2402.00326*, 2024.

[39] Sifan Wang, Shyam Sankaran, and Paris Perdikaris. Respecting causality for training physics-informed neural networks. *Computer Methods in Applied Mechanics and Engineering*, 2024.

[40] Sifan Wang, Shyam Sankaran, Hanwen Wang, and Paris Perdikaris. An expert's guide to training physics-informed neural networks. *arXiv preprint arXiv:2308.08468*, 2023.

[41] Sifan Wang, Xinling Yu, and Paris Perdikaris. When and why pinns fail to train: A neural tangent kernel perspective. *Journal of Computational Physics*, 2022.

[42] Abdul Majid Wazwaz. Partial differential equations: methods and applications. 2002.

[43] R Wille. Karman vortex streets. *Advances in Applied Mechanics*, 1960.

[44] Jian Cheng Wong, Chin Chun Ooi, Abhishek Gupta, and Yew-Soon Ong. Learning in sinusoidal spaces with physics-informed neural networks. *IEEE Transactions on Artificial Intelligence*, 2022.

[45] Chenxi Wu, Min Zhu, Qinyang Tan, Yadhu Kartha, and Lu Lu. A comprehensive study of non-adaptive and residual-based adaptive sampling for physics-informed neural networks. *Computer Methods in Applied Mechanics and Engineering*, 2023.

[46] Haixu Wu, Huakun Luo, Yuezhou Ma, Jianmin Wang, and Mingsheng Long. Ropinn: Region optimized physics-informed neural networks. In *NeurIPS*, 2024.

[47] Yeong-Bin Yang and William McGuire. Stiffness matrix for geometric nonlinear analysis. *Journal of structural engineering*, 1986.

- [48] Jeremy Yu, Lu Lu, Xuhui Meng, and George Em Karniadakis. Gradient-enhanced physics-informed neural networks for forward and inverse pde problems. *Computer Methods in Applied Mechanics and Engineering*, 2022.
- [49] Leo Zhiyuan Zhao, Xueying Ding, and B Aditya Prakash. Pinnsformer: A transformer-based framework for physics-informed neural networks. *ICLR*, 2024.

A Visualization of Gradient Correlation

As a supplement to Figure 1, we provide the visualization for the gradient correlation of all the other standard benchmarks here, where we can obtain the following observations:

- ProPINN generally shows higher gradient correlations than vanilla PINN in all the tasks.
- In PINN, areas with small gradient correlations correspond perfectly to the boundary for higher error zones, indicating the effect of propagation failure.

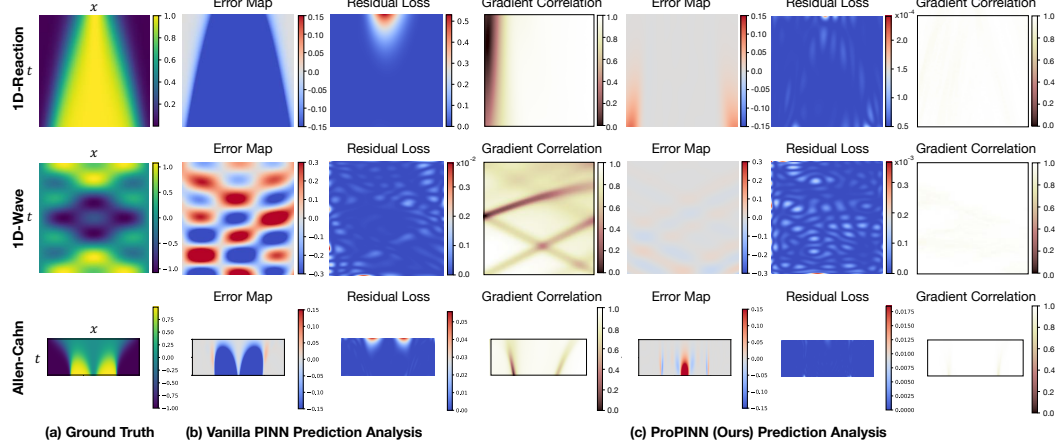


Figure 8: Visualization of gradient correlations on the other three standard benchmarks.

B Visualization of Training Dynamics

We plot the change of gradient correlation, training loss and test error during training in the following.

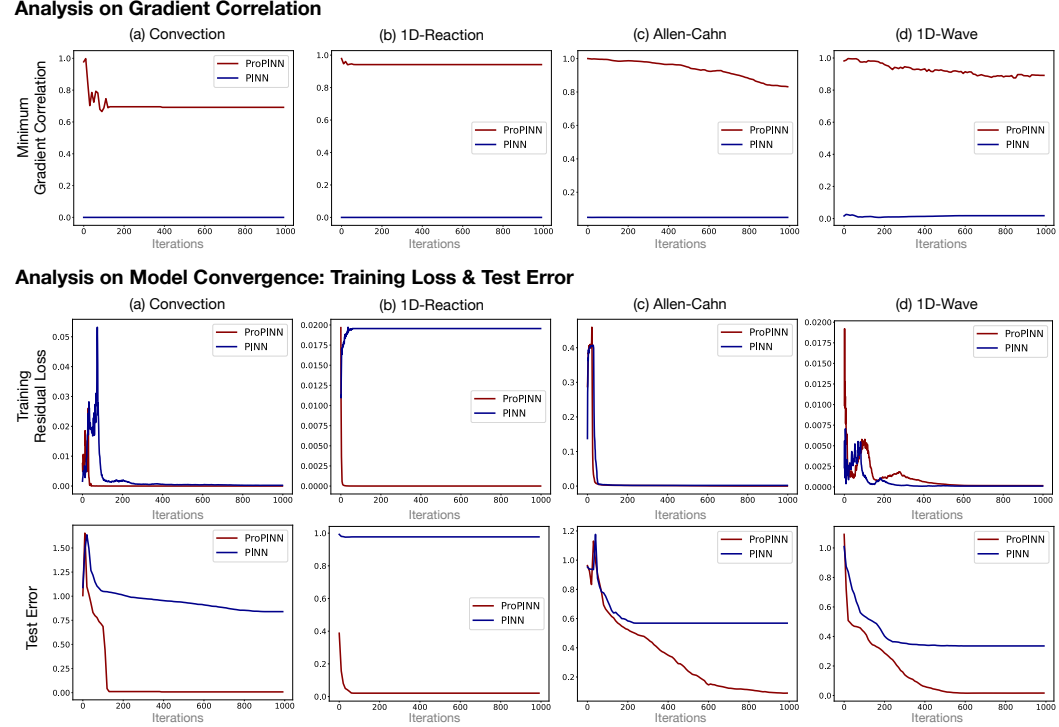


Figure 9: Visualization of training dynamics of ProPINN on all the standard benchmarks.

From the training dynamics presented in Figure 9, we can observe that

- About gradient correlation change: The orthogonal situation of adjacent gradients is progressively getting serious during training. This situation may be because, along with the training process, the model becomes more and more “overfitted” for adjacent points. In other words, the model can deliver quite different optimizing directions to “overfit” two adjacent points independently, resulting in smaller gradient correlations.
- About training loss and test error change: Vanilla PINN is easier to get “converged” (low training loss), while the test error is still relatively high. This comes from that PINN suffers from the propagation failure, which makes its optimization process “get blocked”.

Since this paper mainly focuses on model architecture design, not like NTK-based methods [18] that focus on the training dynamics or convergence properties of PINNs, we would like to leave more in-depth discussion about convergence behavior as our future work.

C Proof of Theorems in the Main Text

This section will present proofs for theorems in Section 3.

C.1 Propagation in FEMs (Theorem 3.1)

This theorem is based on the general formalization of FEMs, which can be directly derived from textbook [10]. Here, we reorganize the formalization to highlight the interaction among solution values of different areas in FEMs.

Proof. Without loss of generality, we consider the following PDE, which is defined in $\Omega \cup \partial\Omega$ with the following constraints:

$$\begin{aligned} \mathcal{F}(u)(\mathbf{x}) &= f(\mathbf{x}), \mathbf{x} \in \Omega; \\ u(\mathbf{x}) &= 0, \mathbf{x} \in \partial\Omega, \end{aligned} \quad (8)$$

where f represents the function of external force. Suppose that the solution $u \in \mathbb{U}$, where $\forall v \in \mathbb{U}, v|_{\partial\Omega} = 0$ and is with corresponding differential property to make the equation constraint \mathcal{F} meaningful, then we can obtain the following variational formalization of PDE in Eq. (8):

$$\int_{\Omega} (\mathcal{F}(u) - f)v dx = 0, \quad \forall v \in \mathbb{U}, \quad (9)$$

where x refers to the variable of one dimension in Ω .

Based on the integration by parts technique, it is easy to derive that

$$\int_{\Omega} (\mathcal{F}(u) - f)v dx = \mathcal{F}'(u)v|_{\partial\Omega} - \int_{\Omega} \mathcal{F}'(u) \frac{\partial v}{\partial x} dx - \int_{\Omega} f v dx = - \int_{\Omega} \mathcal{F}'(u) \frac{\partial v}{\partial x} dx - \int_{\Omega} f v dx, \quad (10)$$

where $\frac{\partial \mathcal{F}'(u)}{\partial x} = \mathcal{F}(u)$. For clarity, we define $D(u, v) = \int_{\Omega} \mathcal{F}'(u) \frac{\partial v}{\partial x} dx$ and $B(v) = - \int_{\Omega} f v dx$. Thus, based on the above variational derivation, the PDE solving process is to find $u \in \mathbb{U}$ to satisfy the following equation:

$$D(u, v) - B(v) = 0, \quad \forall v \in \mathbb{U}. \quad (11)$$

The key idea of FEM is to find an approximated solution on the computation mesh. Specifically, it is to find $\hat{u} \in \hat{\mathbb{U}}$ to satisfy the above-derived constraint, where $\hat{\mathbb{U}}$ is the subspace of \mathbb{U} and essentially a linear space formed by n basis functions $\{\Psi_1, \dots, \Psi_n\}$. Thus, the above variational formalization of PDE can be transformed into an approximated problem, namely, find $\hat{u} \in \hat{\mathbb{U}}$, s.t. $D(\hat{u}, \hat{v}) - B(\hat{v}) = 0, \forall \hat{v} \in \hat{\mathbb{U}}$.

Usually, $\{\Psi_1, \dots, \Psi_n\}$ are defined as the linear interpolation functions of a region, namely:

$$\Psi_i(\mathbf{x}) = \begin{cases} 1 & \text{if } \mathbf{x} = \mathbf{x}_i, \\ \text{Linear - Interpolation}(\mathbf{x}) & \text{if } \mathbf{x} \in \text{Region}(\mathbf{x}_i), \\ 0 & \text{if } \mathbf{x} \in \Omega \setminus \text{Region}(\mathbf{x}_i) \end{cases}, \quad i = 1, \dots, n. \quad (12)$$

$\text{Region}(\mathbf{x}_i)$ denotes the triangular mesh adjacent to \mathbf{x}_i and Ψ_i is zero on the boundary of $\text{Region}(\mathbf{x}_i)$.

Since $\widehat{\mathbb{U}}$ is a linear space formed by n basis functions $\{\Psi_1, \dots, \Psi_n\}$, $\widehat{u} = \sum_{i=1}^n u_i \Psi_i$ and $\widehat{v} = \sum_{i=1}^n v_i \Psi_i$. Thus, the PDE is approximated by solving the following equation set:

$$\sum_{j=1}^n D(\Psi_j, \Psi_i) u_j - B(\Psi_i) = 0, \quad i = 1, \dots, n. \quad (13)$$

It is worth noticing that according to the definition in Eq. (12), basis function Ψ_i is zero in all the other nodes $\mathbf{x}_j, j \neq i$. Thus, the i -th coefficient u_i is also the approximated solution value on node \mathbf{x}_i .

According to the updating strategy of the Jacobi iterative method [13], we can directly obtain:

$$u_j^{(k+1)} = \frac{1}{D(\Psi_j, \Psi_j)} \left(b_j - \sum_{i \neq j} D(\Psi_i, \Psi_j) u_i^{(k)} \right), \quad (14)$$

where $b_j = B(\Psi_j)$ is a constant related to the external force f and $u_j^{(k+1)}$ represents the value of the coefficient at the j -th step, which is also equal to the solution value at the j -th node. \square

C.2 Gradient Correlation (Theorem 3.6)

According to Definition 3.4, if \mathbf{x} and \mathbf{x}' are adjacent and $D_{\text{PINN}}(\mathbf{x}, \mathbf{x}')$, defined in Eq. (4), is less than a empirically defined threshold ϵ , we consider that propagation failure has occurred between \mathbf{x} and \mathbf{x}' . In this theorem, we want to prove that the propagation failure is equivalent to a small gradient correlation $G_{u_\theta}(\mathbf{x}, \mathbf{x}')$ between two adjacent points \mathbf{x} and \mathbf{x}' .

Proof. We notice that the PINN u_θ can be regarded as a multivariate function with respect to the parameters θ and the input variables \mathbf{x} , i.e., $u(\theta, \mathbf{x}) = u_\theta(\mathbf{x})$. Since $u(\theta, \mathbf{x})$ is infinitely differentiable with respect to both θ and \mathbf{x} , and let λ be a sufficiently small step size, we proceed to rewrite the Eq. (4) by employing a Taylor expansion centered at (θ, \mathbf{x}') ,

$$\begin{aligned} D_{\text{PINN}}(\mathbf{x}, \mathbf{x}') &= \lim_{\lambda \rightarrow 0} \frac{\left\| u_\theta(\mathbf{x}') - u_{\theta - \lambda \frac{\partial u_\theta}{\partial \theta}(\mathbf{x}')}(\mathbf{x}') \right\|}{\lambda} \\ &= \lim_{\lambda \rightarrow 0} \frac{\left\| u(\theta, \mathbf{x}') - u(\theta - \lambda \frac{\partial u_\theta}{\partial \theta}(\mathbf{x}), \mathbf{x}') \right\|}{\lambda} \\ &= \lim_{\lambda \rightarrow 0} \frac{\left\| \left\langle \frac{\partial u_\theta}{\partial \theta}(\mathbf{x}'), \lambda \frac{\partial u_\theta}{\partial \theta}(\mathbf{x}) \right\rangle + \mathcal{O}(\lambda^2) \right\|}{\lambda} \\ &= \lim_{\lambda \rightarrow 0} \frac{\lambda G_{u_\theta}(\mathbf{x}, \mathbf{x}') + \mathcal{O}(\lambda^2)}{\lambda} \\ &= G_{u_\theta}(\mathbf{x}, \mathbf{x}'). \end{aligned} \quad (15)$$

Therefore, since the functions $D_{\text{PINN}}(\mathbf{x}, \mathbf{x}')$ and $G_{u_\theta}(\mathbf{x}, \mathbf{x}')$ is equivalent, the sufficient smallness of D guarantees the sufficient smallness of G , and the reverse is also true. \square

It worth noticing that, although $D_{\text{PINN}}(\mathbf{x}, \mathbf{x}')$ and $G_{u_\theta}(\mathbf{x}, \mathbf{x}')$ are numerically equal, they are under different perspectives. Specifically, $D_{\text{PINN}}(\mathbf{x}, \mathbf{x}')$ is derived based on the physical meaningful of FEMs, which can perfectly reflect the definition of “stiffness matrix”, namely the affect to position \mathbf{x}' when \mathbf{x} has a unit displacement or force. In contrast, the definition of $G_{u_\theta}(\mathbf{x}, \mathbf{x}')$ describes the property of PINN models, which provides a clearer understanding in the deep learning context.

C.3 Gradient Correlation Improvement (Theorem 3.8)

This theorem demonstrates that uniting region gradients can boost the gradient correlation among nearby points. This theorem can be proved under the Assumption 3.7, which assumes the positive gradient correlation of nearby points.

Proof. To demonstrate the effectiveness of uniting region gradients, it is equivalent to proving that,

$$\begin{aligned}
& G_{u_\theta}(\mathbf{x}, \mathbf{x}') \leq G_{u_\theta^{\text{region}}}(\mathbf{x}, \mathbf{x}') \\
\Leftrightarrow & G_{u_\theta}(\mathbf{x}, \mathbf{x}') \leq G_{u_\theta(\mathbf{x}) + \frac{1}{k} \sum_{i=1}^k u_\theta(\mathbf{x} + \boldsymbol{\delta}_i)}(\mathbf{x}, \mathbf{x}') \\
\Leftrightarrow & \left\| \left\langle \frac{\partial u_\theta}{\partial \theta} \Big|_{\mathbf{x}}, \frac{\partial u_\theta}{\partial \theta} \Big|_{\mathbf{x}'} \right\rangle \right\| \leq \left\| \left\langle \left(\frac{\partial u_\theta}{\partial \theta}(\mathbf{x}) + \frac{1}{k} \sum_{i=1}^k \frac{\partial u_\theta}{\partial \theta}(\mathbf{x} + \boldsymbol{\delta}_i), \frac{\partial u_\theta}{\partial \theta}(\mathbf{x}') + \frac{1}{k} \sum_{i=1}^k \frac{\partial u_\theta}{\partial \theta}(\mathbf{x}' + \boldsymbol{\delta}_i) \right) \right\rangle \right\| \\
\Leftrightarrow & \left\langle \frac{\partial u_\theta}{\partial \theta}(\mathbf{x}), \frac{\partial u_\theta}{\partial \theta}(\mathbf{x}') \right\rangle \leq \left\| \left\langle \left(\frac{\partial u_\theta}{\partial \theta}(\mathbf{x}) + \frac{1}{k} \sum_{i=1}^k \frac{\partial u_\theta}{\partial \theta}(\mathbf{x} + \boldsymbol{\delta}_i), \frac{\partial u_\theta}{\partial \theta}(\mathbf{x}') + \frac{1}{k} \sum_{i=1}^k \frac{\partial u_\theta}{\partial \theta}(\mathbf{x}' + \boldsymbol{\delta}_i) \right) \right\rangle \right\| \tag{16}
\end{aligned}$$

Here the third \Leftrightarrow is due to the condition that $\|\mathbf{x} - \mathbf{x}'\| \leq \frac{R}{3}$, thus $\left\langle \frac{\partial u_\theta}{\partial \theta}(\mathbf{x}), \frac{\partial u_\theta}{\partial \theta}(\mathbf{x}') \right\rangle \geq 0$.

From the pre-defined perturbations $\{\boldsymbol{\delta}_i\}_{i=1}^k$ with $\|\boldsymbol{\delta}_i\| \leq \frac{R}{3}$ and the given \mathbf{x} and \mathbf{x}' such that $\|\mathbf{x} - \mathbf{x}'\| \leq \frac{R}{3}$, it follows that,

$$\|(\mathbf{x} + \boldsymbol{\delta}_i) - \mathbf{x}'\| \leq R, \quad \|\mathbf{x} - (\mathbf{x}' + \boldsymbol{\delta}_j)\| \leq R, \quad \|(\mathbf{x} + \boldsymbol{\delta}_i) - (\mathbf{x}' + \boldsymbol{\delta}_j)\| \leq R, \quad \forall i, j \in \{1, \dots, k\}. \tag{17}$$

Given the choice of R in Assumption 3.7, we obtain that

$$\begin{aligned}
& \left\| \left\langle \left(\frac{\partial u_\theta}{\partial \theta}(\mathbf{x}) + \frac{1}{k} \sum_{i=1}^k \frac{\partial u_\theta}{\partial \theta}(\mathbf{x} + \boldsymbol{\delta}_i), \frac{\partial u_\theta}{\partial \theta}(\mathbf{x}') + \frac{1}{k} \sum_{i=1}^k \frac{\partial u_\theta}{\partial \theta}(\mathbf{x}' + \boldsymbol{\delta}_i) \right) \right\rangle \right\| \\
&= \left\langle \frac{\partial u_\theta}{\partial \theta}(\mathbf{x}), \frac{\partial u_\theta}{\partial \theta}(\mathbf{x}') \right\rangle + \left\langle \frac{\partial u_\theta}{\partial \theta}(\mathbf{x}), \frac{1}{k} \sum_{i=1}^k \frac{\partial u_\theta}{\partial \theta}(\mathbf{x}' + \boldsymbol{\delta}_i) \right\rangle \\
&+ \left\langle \frac{1}{k} \sum_{i=1}^k \frac{\partial u_\theta}{\partial \theta}(\mathbf{x} + \boldsymbol{\delta}_i), \frac{\partial u_\theta}{\partial \theta}(\mathbf{x}') \right\rangle + \left\langle \frac{1}{k} \sum_{i=1}^k \frac{\partial u_\theta}{\partial \theta}(\mathbf{x} + \boldsymbol{\delta}_i), \frac{1}{k} \sum_{i=1}^k \frac{\partial u_\theta}{\partial \theta}(\mathbf{x}' + \boldsymbol{\delta}_i) \right\rangle \\
&\geq \left\langle \frac{\partial u_\theta}{\partial \theta}(\mathbf{x}), \frac{\partial u_\theta}{\partial \theta}(\mathbf{x}') \right\rangle.
\end{aligned} \tag{18}$$

Consequently, the conclusion in Eq. (16) and Theorem 3.8 has been proven. \square

C.4 Justification of Assumption 3.7

Theoretical understanding Firstly, we want to highlight that if we change the positive constraint of region size R in the assumption to “non-negative”, Assumption 3.7 is always true. This can be directly proved by the following derivation:

$$\left\langle \frac{\partial u_\theta}{\partial \theta} \Big|_{\mathbf{x}}, \frac{\partial u_\theta}{\partial \theta} \Big|_{\mathbf{x}} \right\rangle \geq 0. \tag{19}$$

Further, we still consider the positive constraint of region size R . If $\|\frac{\partial u_\theta}{\partial \theta} \Big|_{\mathbf{x}}\| \neq 0$ at \mathbf{x} , then $\left\langle \frac{\partial u_\theta}{\partial \theta} \Big|_{\mathbf{x}}, \frac{\partial u_\theta}{\partial \theta} \Big|_{\mathbf{x}} \right\rangle > 0$. According to the boundedness of $\frac{\partial^2 u_\theta}{\partial \theta \partial \mathbf{x}}$, there must exist a region $R_{\mathbf{x}} = \left\langle \frac{\partial u_\theta}{\partial \theta} \Big|_{\mathbf{x}}, \frac{\partial u_\theta}{\partial \theta} \Big|_{\mathbf{x}} \right\rangle > 0$ s.t. $\forall \mathbf{x}' \in \Omega$, if $\|\mathbf{x}' - \mathbf{x}\| \leq R_{\mathbf{x}}$, we have

$$\begin{aligned}
\left\langle \frac{\partial u_\theta}{\partial \theta} \Big|_{\mathbf{x}}, \frac{\partial u_\theta}{\partial \theta} \Big|_{\mathbf{x}'} \right\rangle &= \left\langle \frac{\partial u_\theta}{\partial \theta} \Big|_{\mathbf{x}}, \frac{\partial u_\theta}{\partial \theta} \Big|_{\mathbf{x}} + (\mathbf{x}' - \mathbf{x}) \frac{\partial^2 u_\theta}{\partial \theta \partial \mathbf{x}} + \mathcal{O}((\mathbf{x}' - \mathbf{x})^2) \right\rangle \\
&\geq \left\langle \frac{\partial u_\theta}{\partial \theta} \Big|_{\mathbf{x}}, \frac{\partial u_\theta}{\partial \theta} \Big|_{\mathbf{x}} \right\rangle - R_{\mathbf{x}} \left\langle \frac{\partial u_\theta}{\partial \theta} \Big|_{\mathbf{x}}, \frac{\partial^2 u_\theta}{\partial \theta \partial \mathbf{x}} \right\rangle \\
&= \frac{1}{2} \left\langle \frac{\partial u_\theta}{\partial \theta} \Big|_{\mathbf{x}}, \frac{\partial u_\theta}{\partial \theta} \Big|_{\mathbf{x}} \right\rangle \\
&> 0.
\end{aligned} \tag{20}$$

Thus, the unguaranteed part in Assumption 3.7 is $R = \min_{\mathbf{x} \in \Omega} R_{\mathbf{x}} > 0$, namely *is there a unified region size for all collocation points*. The following experiment statistics can well verify this question.

Experimental statistics We also count the proportion of points that satisfy Assumption 3.7 in each PDE. Specifically, we take 10^4 equally spaced points at each PDE. For each collocation point, we consider its gradient correlation with nearby points, whose distance is around 10^{-2} . As presented in Table 4, if we set R as 10^{-2} , we can find all the collocation points are under positive region gradient correlation, indicating that Assumption 3.7 can be well guaranteed in practice.

Table 4: Statistics for Assumption 3.7.

Statistics of 10^4 Points	Convection	1D-Reaction	Allen-Cahn	1D-Wave
Positive Ratio of region Gradient Correlations	100%	100%	100%	100%

D Implementation Details

In this section, we will provide details about benchmarks, experiment settings, model configurations and evaluation metrics.

D.1 Benchmark Description

As shown in Figure 10, we evaluate ProPINN on six tasks, which include four standard benchmarks: Convection, 1D-Reaction, Allen-Cahn and 1D-Wave and two complex physics modeling tasks: Karman Vortex and Fluid Dynamics. Here are the details of each benchmark.

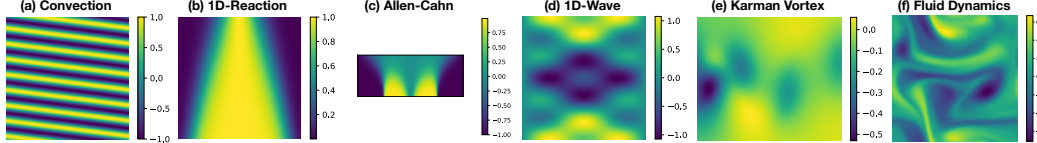


Figure 10: Summary of benchmarks. We visualize the solution map of each PDE-solving task.

Convection This problem describes a hyperbolic PDE, which can be formalized as follows:

$$\begin{aligned} \text{Equation constraint: } & \frac{\partial u}{\partial t} + \beta \frac{\partial u}{\partial x} = 0, \quad x \in (0, 2\pi), t \in (0, 1), \\ \text{Initial condition: } & u(x, 0) = \sin(x), \quad x \in [0, 2\pi], \\ \text{Boundary condition: } & u(0, t) = u(2\pi, t), \quad t \in [0, 1], \end{aligned} \tag{21}$$

where the convection coefficient β is set as 50. Its analytic solution is $u(x, t) = \sin(x - \beta t)$. As presented in Figure 10(a), this problem involves rapid variations along the temporal dimension, making it hard for neural networks to approximate. Thus, this problem is widely tested in characterizing PINN failure modes [22] and evaluating new architectures [49, 26, 46].

1D-Reaction This problem is about a non-linear PDE for chemical reactions, whose equation is formalized as follows:

$$\begin{aligned} \text{Equation constraint: } & \frac{\partial u}{\partial t} - \rho u(1 - u) = 0, \quad x \in (0, 2\pi), t \in (0, 1), \\ \text{Initial condition: } & u(x, 0) = \exp\left(-\frac{(x - \pi)^2}{2(\pi/4)^2}\right), \quad x \in [0, 2\pi], \\ \text{Boundary condition: } & u(0, t) = u(2\pi, t), \quad t \in [0, 1], \end{aligned} \tag{22}$$

where the PDE coefficient ρ is set as 5. The analytic solution for this PDE is $u(x, t) = \frac{h(x)e^{\rho t}}{h(x)e^{\rho t} + 1 - h(x)}$, where $h(x) = \exp\left(-\frac{(x - \pi)^2}{2(\pi/4)^2}\right)$. As shown in Figure 10(b), this task presents rapid variations in some areas, making it hard to solve [22]. We experimented with this problem following PINNsFormer [49].

Allen-Cahn This problem is a typical reaction-diffusion equation, which is defined as:

$$\begin{aligned}
\text{Equation constraint: } & \frac{\partial u}{\partial t} - 0.0001 \frac{\partial^2 u}{\partial x^2} + 5u^3 - 5u = 0, \quad x \in (-1, 1), t \in (0, 1), \\
\text{Initial condition: } & u(x, 0) = x^2 \cos(\pi x), \quad x \in [-1, 1], \\
\text{Boundary condition: } & u(-1, t) = u(1, t), \quad t \in [0, 1], \\
\text{Boundary condition: } & \frac{\partial u(-1, t)}{\partial x} = \frac{\partial u(1, t)}{\partial x}, \quad t \in [0, 1].
\end{aligned} \tag{23}$$

Since this PDE does not have an analytic solution, following previous studies [28], we adopt the results pre-calculated by traditional spectral methods [21] as the reference. As illustrated in Figure 10(c), this task also includes the sharp area, making it usually studied as PINN failure modes [22].

1D-Wave This problem is a hyperbolic PDE, which involves high-order derivatives in its equation constraint. The exact governing equation is defined as follows:

$$\begin{aligned}
\text{Equation constraint: } & \frac{\partial^2 u}{\partial t^2} - 4 \frac{\partial^2 u}{\partial x^2} = 0, \quad x \in (0, 1), t \in (0, 1), \\
\text{Initial condition: } & u(x, 0) = \sin(\pi x) + \frac{1}{2} \sin(\beta \pi x), \quad x \in [0, 1], \\
\text{Initial condition: } & \frac{\partial u(x, 0)}{\partial t} = 0, \quad x \in [0, 1], \\
\text{Boundary condition: } & u(0, t) = u(1, t) = 0, \quad t \in [0, 1],
\end{aligned} \tag{24}$$

where its periodic coefficient β is set as 3 and the analytic solution is $u(x, t) = \sin(\pi x) \cos(2\pi t) + \frac{1}{2} \sin(\beta \pi x) \cos(2\beta \pi t)$. This solution presents periodic patterns, which require the neural network to fit a periodic output space (Figure 10(d)).

Karman Vortex This task describes the incompressible fluid moving past a cylinder, which involves the famous Karman vortex street phenomenon [43] as shown in Figure 10(e) and is governed by the following Navier-Stokes equations:

$$\begin{aligned}
\frac{\partial u}{\partial t} + (u \frac{\partial u}{\partial x} + v \frac{\partial u}{\partial y}) &= -\frac{\partial p}{\partial x} + 0.01(\frac{\partial^2 u}{\partial x^2} + \frac{\partial^2 u}{\partial y^2}) \\
\frac{\partial v}{\partial t} + (u \frac{\partial v}{\partial x} + v \frac{\partial v}{\partial y}) &= -\frac{\partial p}{\partial y} + 0.01(\frac{\partial^2 v}{\partial x^2} + \frac{\partial^2 v}{\partial y^2}) \\
\frac{\partial u}{\partial x} + \frac{\partial v}{\partial y} &= 0,
\end{aligned} \tag{25}$$

where u, v represent the velocity along the x-axis and y-axis. p denotes the pressure field. Since we cannot obtain the analytic solution of the Navier-Stokes equations, we experiment with the high-resolution data calculated by the spectral/hp-element solver NekTar [19] following [28].

Specifically, the generated fluid sequence contains 200 frames. The task is to reconstruct the pressure field p with physics loss defined in the above, which contains the above three equations and the supervision of ground truth velocity.

Fluid Dynamics This problem is from the well-established PINN framework JAX-PI [40], using the 2D incompressible Navier-Stokes equations in fluid dynamics and appropriate initial conditions to simulate fluid flow in a torus. The governed PDEs and initial conditions we used are shown as:

$$\begin{aligned}
\frac{\partial w}{\partial t} + (u \frac{\partial w}{\partial x} + v \frac{\partial w}{\partial y}) &= \frac{1}{\text{Re}} (\frac{\partial^2 w}{\partial x^2} + \frac{\partial^2 w}{\partial y^2}), \quad (t, x, y) \in [0, T] \times \Omega \\
\frac{\partial u}{\partial x} + \frac{\partial v}{\partial y} &= 0, \quad (t, x, y) \in [0, T] \times \Omega \\
w(0, x, y) &= w_0(x, y), \quad (x, y) \in \Omega
\end{aligned} \tag{26}$$

where $\mathbf{u} = (u, v)$ is the two-dimensional velocity vector of the fluid, $w = \nabla \times \mathbf{u}$ is the fluid vorticity, with T set to 10s, Ω set to $[0, 2\pi]^2$, and the Reynolds number Re set to 100. w_0 denotes the given initial condition of vorticity.

The task is to simulate the future 10 seconds of fluid vorticity field w solely based on the initial condition. However, the convective term $(\mathbf{u} \cdot \nabla)\mathbf{u}$ in the Navier-Stokes equations is nonlinear, which can lead to chaotic behavior. Thus, small changes in initial conditions can result in significantly different outcomes, making this task extremely difficult [8]. As presented in Figure 10(f), the physics field in this task is quite complex.

D.2 Experiment Settings

We repeat all the experiments three times and report the average performance in the main text. All the experiments are conducted on a single A100 40GB GPU. Here are detailed configurations for each benchmark. The standard deviations can be found in Appendix H.

Standard benchmarks For Convection, 1D-Reaction and 1D-Wave, we follow the experiment settings in PINNsFormer [49]. Specifically, each experiment selects 101×101 collocation points in the input domain and sets loss weights $\lambda_* = 1$. All the models are trained with L-BFGS optimizer [23] for 1,000 iterations in PyTorch [27]. As for Allen-Cahn, we also implement this PDE in PyTorch with all the configurations same as PINNsFormer but set $\lambda_{\text{res}} = \lambda_{\text{bc}} = 1$ and $\lambda_{\text{ic}} = 10$ for all models to fit the complex initial condition.

Karman Vortex As we stated before, this task is supervised by the equation constraints and ground truth of velocity. Concretely, we randomly select 2500 collocation points from the whole spatiotemporal sequence and train the model with L-BFGS optimizer for 1,000 iterations in PyTorch with loss weights $\lambda_* = 1$ following PINNsFormer [49].

Fluid Dynamics In this task, we use the JAX-PI framework¹. Here are the detailed settings. Firstly, to tackle the long temporal interval, we split the temporal domain into 10 windows and each window is trained separately in sequence. For each window, a total of 150,000 training steps are used, with each training step sampling uniformly distributed points in both the temporal and spatial domains, totaling 4096 coordinates (t, x, y) . Then, the corresponding governed PDEs and initial conditions (Eq. (26)) are used as loss functions for training. Specifically, for the first window, the initial condition is the value of the exact solution at the beginning time, and subsequent windows use the solution at the last timestamp from the previous window as the initial condition. Although this time-marching strategy may lead to error accumulation due to the setting of initial conditions, excellent models and training methods can maintain very low relative errors even in the last window. Note that JAX-PI also utilizes some tricks to ensure the final performance, such as random Fourier feature embedding [33]. We also maintain these tricks in all the models to ensure that the only variable is model architecture for rigorous comparison. In this task, we use Adam [20] with a learning rate of 0.001 for optimization.

D.3 Model Configuration

ProPINN As highlighted in the main text, we insist on the lightweight design in ProPINN. Specifically, the projection layer \mathcal{P} involves two linear layers with an in-between activation function, where the input dimension $(d+1)$ is firstly projected to 8 and then to 32, which is the same as the embedding size of PINNsFormer [49]. And the multi-region mixing layer \mathcal{M} also involves two linear layers with an in-between activation, which is only applied to the region dimension. Specifically, \mathcal{M} will first project the $\# \text{scale}$ scales to 8 and then to 1 after an activation layer. As for the final projection layer \mathcal{H} , it consists of three linear layers with inner activations, whose hidden dimension is set as 64.

Baselines In our experiments, we also compare ProPINN with seven baselines. Here are our implementation details for these baselines:

- For vanilla PINN [28], QRes [7], FLS [44] and PINNsFormer [49], we follow the PyTorch implementation of these models provided in PINNsFormer and reimplement them in JAX to fit the Fluid Dynamics task in JAX-PI [40]. Specifically, vanilla PINN, QRes and FLS are all with 4 layers with 512 hidden channels. PINNsFormer contains 1 encoder layer and 1 decoder layer with 32 hidden channels for the attention mechanism and 512 hidden channels for the feedforward layer.

¹<https://github.com/PredictiveIntelligenceLab/jaxpi>

- As for SetPINN [26], we implement this model based on their official paper, which can reproduce the results reported in their paper. Also, we reimplement it in JAX for the Fluid Dynamics task. Specifically, same to the official configuration in PINNsFormer, SetPINN is experimented with 1 encoder layer and 1 decoder layer, which contains 32 hidden channels for the attention mechanism and 512 hidden channels for the feedforward layer.
- For KAN [24], we adopt their official code and set hyperparameters following [46].
- For PirateNet [38], its official implementation is in JAX. Thus, we directly test their official version in the Fluid Dynamics task and reimplement it in PyTorch for other benchmarks. Specifically, it contains 256 hidden channels for representations and 4 layers following its official configuration.

Reproduction of baselines For all baselines, we made a great effort to reproduce their performance. Especially, the above-mentioned hyperparameters can perfectly reproduce their official results. Thus, in the shared tasks, we directly report the official results of baselines. As for new tasks (e.g. Allen-Cahn, Fluid Dynamics) without official performance of baselines, we use the same configuration as the previous reproduction. Notably, ProPINN adopts the same model configuration for all PDEs. Thus, the comparison is fair and rigorous.

D.4 Metrics

As we stated before, we evaluate the model-predicted solution based on relative L1 error (rMAE) and relative Root Mean Square Error (rRMSE). For ground truth u and model prediction u_θ , these two metrics can be calculated as follows:

$$\text{rMAE: } \sqrt{\frac{\sum_{i=1}^n |u_\theta(\mathbf{x}_i) - u(\mathbf{x}_i)|}{\sum_{i=1}^n |u(\mathbf{x}_i)|}} \quad \text{rRMSE: } \sqrt{\frac{\sum_{i=1}^n (u_\theta(\mathbf{x}_i) - u(\mathbf{x}_i))^2}{\sum_{i=1}^n (u(\mathbf{x}_i))^2}}, \quad (27)$$

where $\{\mathbf{x}_i\}_{i=1}^n$ are selected collocation points for evaluation.

E Hyperparameter Analysis

As a supplement to ablations in Figure 7 of the main text, we also test the model performance under different hyperparameter configurations, including the number of perturbations at each scale (k_1, k_2, k_3), size of perturbation region (R_1, R_2, R_3) and the number of scales #scale. The results are presented in Figure 11, where we can obtain the following observations.

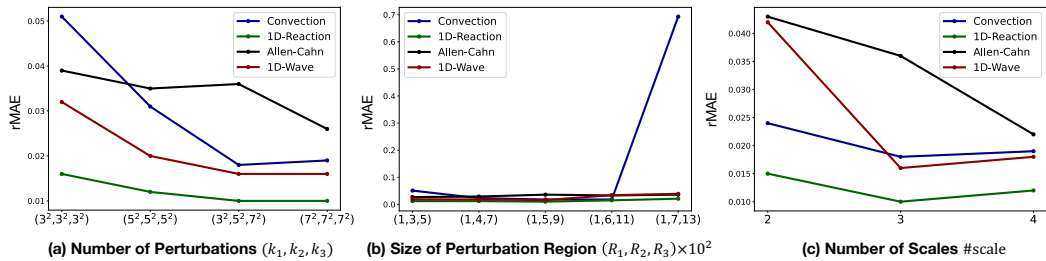


Figure 11: Model analysis with respect to different hyperparameter configurations of ProPINN. For (c), two scales correspond to $(R_1, R_2) = (0.01, 0.05)$ and four scales correspond to $(R_1, R_2, R_3, R_4) = (0.01, 0.03, 0.07, 0.09)$.

(1) *More perturbations will generally boost the model performance.* As stated in Section 3.2, we adopt differential perturbation to unite gradients of region points. Thus, adding perturbation points will enhance the connection of region gradients, thereby benefiting the final performance, while this will also bring more computation costs. Thus, we choose $(k_1, k_2, k_3) = (3^2, 5^2, 7^2)$ for a better trade-off between efficiency and performance.

(2) *The size of the perturbation region is up to the PDE property.* As Remark 3.5 discussed, the gradient correlations only consider the points within a region. Therefore, in the Convection equation that involves the rapid variation in the PDE solution, enlarging the perturbation size to $R_3 = 0.13$

(the whole domain is $[0, 2\pi] \times [0, 1]$) may introduce noise to the learning process, making the final performance degenerate seriously. Also, it is observed that ProPINN performs relatively steadily on all other benchmarks in different perturbation regions. Thus, we believe the effect of this hyperparameter is up to a certain PDE. And our design in choosing (R_1, R_2, R_3) as $(0.01, 0.05, 0.09)$ can be a generalizable choice.

(3) *Adding scales can also boost the model performance.* As shown in Figure 7 of the main text, only one scale in ProPINN will bring a serious performance drop. Further, in Figure 11(c), we increase the number of scales from 2 to 4. It is observed that the model performance is generally improved, especially for Allen-Cahn, which is with a complex solution, thereby can benefit more from adding scales. These results further demonstrate the effectiveness of our design in multi-region mixing.

F More Ablations

As a supplement to Figure 7, we provide more ablations on model performance and design here.

Performance under aligned efficiency As shown in Figure 5, some single-point-processing architectures, such as vanilla PINN, may present very significant speed. To ensure a more comprehensive comparison, we also include the performance comparison under the aligned efficiency, where we increase the number of layers and the training iterations. From Table 5, we can find that adding layers cannot improve the final performance. Actually, as presented in Figure 7(d) of the main text, PINN fails when scaling up the model size. That is why a larger model will bring worse performance in the following experiments. About training iterations, as discussed in this paper, PINN suffers from propagation failure, which means some areas cannot receive the correct supervision; that is why increasing the training iterations does not bring benefits to PINN.

Table 5: Model performance under aligned efficiency. To ensure a comprehensive comparison, we further test Vanilla PINN under more training iterations and more layers.

Convection rMAE	Training Iterations			Model Efficiency	
	1000 iters	2000 iters	4000 iters	GPU Memory (GB)	s / 1000iters
Vanilla PINN	0.778	0.778	0.778	1.06	18.62
Vanilla PINN + 2 Layers	0.825	0.825	0.825	2.00	39.09
ProPINN	0.018	0.008	0.008	1.72	37.76

Adopt other types of optimizers In this paper, we strictly follow the well-established benchmarks and L-BFGS for standard benchmarks and Karman Vortex, Adam for Fluid Dynamics, which is the same as the previous research [26] and JAX-PI. All the baselines and ProPINN are under the same training strategy to ensure a fair comparison. Actually, there are other choices of optimizers, such as the combination of Adam and L-BFGS. To ensure a comprehensive comparison, we also compare different models under the Adam+L-BFGS setting. As shown below, under this new choice of Adam+L-BFGS, ProPINN is still the best model across all four benchmarks. Besides, comparing Table 6 and Table 2, we can find that pure L-BFGS can already achieve a good performance for all models. Since this paper only focuses on the model architecture rather than PINN optimizers, we would like to leave more discussion about optimizers as our future work.

Table 6: Model comparison under the Adam+L-BFGS setting, where we first train the model with Adam for 100 iterations and then optimize the model with L-BFGS for 1000 iterations.

Model rRMSE under Adam+L-BFGS	Convection	1D-Reaction	Allen-Cahn	1D-Wave
Vanilla PINN [28]	0.823	0.982	0.576	0.381
QRes [7]	0.852	0.573	0.957	<u>0.178</u>
FLS [44]	0.693	0.049	0.651	<u>0.186</u>
KAN [24]	0.873	0.057	0.581	0.221
PirateNet [38]	1.294	0.046	<u>0.136</u>	0.511
PINNsFormer [49]	0.032	<u>0.027</u>	0.532	0.489
SetPINN [26]	<u>0.031</u>	0.046	0.597	0.332
ProPINN (Ours)	0.020	0.020	0.087	0.016
Promotion	35%	26%	36%	91%

Adopt gradient correlation as regularization term As stated in Theorem 3.6, we prove that the root cause of propagation failure is a lower gradient correlation. Thus, it is a trivial solution to add gradient correlation as a regularization term for the PINN loss. Note that gradient correlation needs to calculate the gradients of model parameters on different collocation points $\frac{\partial u_\theta}{\partial \theta}(x)$. Firstly, it will take around 60s on a single A100 GPU to calculate gradient correlations of 10000 points of Convection in each step. Secondly, the optimization of gradient correlation loss will require calculating the second-order derivative of model parameters. Thus, we do not think this is a practical design.

Table 7: Comparison between ProPINN and gradient-correlation regularization term on Convection.

Model	rMAE	GPU Memory (GB)	Running Time (s/1000iters)
Vanilla PINN [28]	0.778	1.06	18.62
Vanilla PINN [28] + Gradient Correlation Loss	0.528	2.31	65.17
ProPINN (Ours)	0.018	1.72	37.76

Here, we do some simplification to enable training of adding gradient correlation as a regularization term. Specifically, we split the collocation points into two interlaced sets and add gradient correlation between these two sets as a regularization term with a weight of 0.001. As shown in Table 7, this design is slightly better than PINN, but it is more time-consuming and worse than ProPINN.

Other architecture choices to improve gradient correlation PINNsFormer [26] and SetPINN [26] explicitly capture the correlation among different collocation points. As shown in Table 2 and Figure 5, these two models cannot beat ProPINN in performance and efficiency. This may be because these two models only consider the “representation correlation”, not the “gradient correlation”.

Actually, we cannot figure out new architectures different from ProPINN that can guarantee gradient correlation (Theorem 3.8) and balance performance and efficiency. Thus, we believe that ProPINN is a favorable and theoretically guaranteed choice to enhance gradient correlation among nearby points.

G More Showcases

In the main text, we have already provided the visualization comparison on Convection and 1D-Wave in Figure 4 and Fluid Dynamics in Figure 6. Here we also provide comparisons of the other three benchmarks in Figure 12 and Figure 13.

It is easy to observe that ProPINN is better than PINNsFormer in handling the areas with rapid variations, including the corner of 1D-Reaction, the middle region of Allen-Cahn and the vortex of Karman Vortex, which come from its better propagation property. Besides, we can find that PirateNet under the single-point-processing paradigm fails to capture the vortex dynamics, indicating the inherent deficiency of single-point-processing models in complex physics simulations.

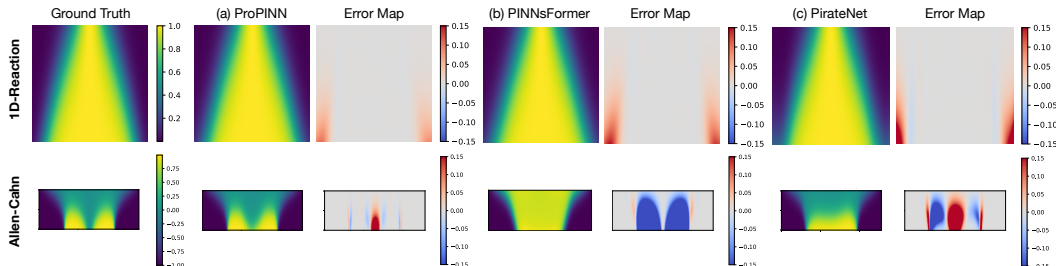


Figure 12: Visualizations of model approximated solution on the 1D-Reaction and Allen-Cahn benchmarks. Error map ($u_\theta - u$) is also plotted.

H Standard Deviations

All the experiments are repeated three times and the standard deviations are listed in Table 8. We can find that in all benchmarks, ProPINN surpasses the second-best model with high confidence.



Figure 13: Comparison of model approximated solutions on the Karman Vortex benchmark. Error map ($u_\theta - u$) is also plotted.

Table 8: Standard deviations of ProPINN. We also list the performance of the second-best model. P-value < 0.05 indicates that ProPINN surpasses the second-best model with high confidence.

rMAE	Standard Benchmarks				Complex Physics	
	Convection	1D-Reaction	Allen-Cahn	1D-Wave	Karman Vortex	Fluid Dynamics
Second-best Model	0.023 ± 0.002 (PINNsFormer)	0.015 ± 0.002 (PINNsFormer)	0.098 ± 0.007 (PirateNet)	0.051 ± 0.008 (PirateNet)	0.287 ± 0.08 (SetPINN)	0.2362 ± 0.013 (FLS)
ProPINN	0.018 ± 0.001	0.010 ± 0.001	0.036 ± 0.006	0.016 ± 0.004	0.161 ± 0.03	0.1834 ± 0.010
P-Value	0.015	0.015	0.000	0.001	0.026	0.003

I Limitations and Future Work

One potential limitation of ProPINN lies in its application to extremely high-dimensional PDEs, such as the Hamilton-Jacobi-Bellman equation in optimal control [4] and the Schrodinger equation in quantum physics [5], which may involve millions of dimensions. These high-dimensional PDE-solving tasks will require the model to augment many points within each region, which may bring a huge computation overload for multi-region mixing.

This limitation can be resolved by integrating the “amortization” technique [17, 31, 16] with ProPINN, which can “amortize the computation over the optimization process via randomization”. Since this paper mainly focuses on propagation failures of PINNs instead of high-dimensional issues and we have conducted extensive experiments in PINN failure modes and complex physics to verify the model effectiveness, we would like to leave the topic as our future work. Also, we would like to highlight that the favorable results in solving Navier-Stokes equations are already valuable for extensive real-world applications, such as aerodynamic simulation [25].

J Broader Impacts

This paper provides an in-depth study of the propagation failure in PINNs, which is a crucial phenomenon of PINN optimization. We formally prove that the root cause of propagation failure is the lower gradient correlation, which can be inspiring for future research. Also, we present ProPINN as a practical PINN architecture with favorable efficiency and significant promotion over the previous methods. More importantly, ProPINN performs well in solving complex Navier-Stokes equations, which can be valuable for real-world applications. Since we purely focus on the research problem of PINNs, there are no potential negative social impacts or ethical risks.